eman ta zabal zazu

Universidad Euskal Herriko
del País Vasco Unibertsitatea

ZIENTZIA
ETA TEKNOLOGIA
FAKULTATEA

FACULTAD
DE CIENCIA
Y TECNOLOGÍA

Gradu Amaierako Lana / Trabajo Fin de Grado
Fisikako Gradua / Grado en Física

An in-orbit Diagnostic System for Electric Propulsion Thrusters through Interferometry

Egilea/Autor/a:
Eneko Lekuona Ugalde
Zuzendaria/Director/a:
Aitziber Anakabe Iturriaga

Leioa, 2019ko uztailaren 22a /Leioa, 22 de julio de 2019

Contents

1 Introduction and Objectives

This report describes the ORBITA project in which I have worked for AVS (Added Value Solutions) UK. The project was supported by the UK Space Agency and the European Space Agency (ESA), where the second also provided funding and offered their facilities for testing. At its core, the project had the advancement of the technology of electric thruster diagnostics as its objective. It was found in market analysis that no device exists that performs diagnostics on electric thrusters in orbit, and therefore, it was decided to pursue the development of such. Receiving thruster performance measurements during mission can allow fine-tuning of the thruster parameters, which would increase its lifetime or improve its efficiency.

After the first stages of the project, consisting of a market analysis and a trade-off of different diagnostic techniques for electric propulsion devices, my involvement begun in the development stage. A Fabry-Pérot interferometer was chosen as the diagnostic technology to be developed. By measuring the frequency of the Doppler shifted light emitted by the xenon plasma plume of an electric propulsion device, its exhaust velocity could be calculated. I fulfilled a secondary role in the mechanical design, where I aided and gave advice to the colleague responsible for this part. With the optical system, my involvement also included the procurement of components from the manufacturers, ensuring their compatibility with our device. However, my main tasks were related to software development. I wrote a Python program that controls rotational stages key to the interferometer, while also taking measurements and saving them, automatizing the most repeated steps in the operation of the device. Based on simulations of data expected to measure in testing, I also wrote the program responsible of processing the data, to extract the exhaust velocity from it, and integrated both programs. Finally, I also made the proof-of-concept version of a secondary system that involves an Arduino board and an stepper motor.

In the design of a breadboard version of a diagnostic device, my personal objective was to ensure the correct functioning of the parts of the system entrusted to me, as well as helping the rest of the team at my fullest capacity for the whole system to give satisfactory results when testing.

In this text, the theoretical framework necessary to understand the project and why the parameters that it measures can be of interest will be introduced. Then, after a more detailed explanation of the project, the developed system's main parts will be explained, with added emphasis on the programs developed by myself. Finally, the performed test will be described, including the results obtained and the conclusion that were taken from them.

2 Theoretical Framework

2.1 Propulsion theory

To understand the project, first it must be made clear why the measurement of the exhaust velocity can be of interest, as well as what makes electric propulsion different from other conventional methods and worth developing such systems for.

Virtually all rocket and satellite propulsion methods involve in one way or another the acceleration and ejection of some propellant mass. It is to be expected from basic physical intuition for the performance of this method to be dependant of the ejected mass and its velocity. This is described by what is known as the "rocket equation", which can be derived starting from Newton's laws of motion: the force applied on the spacecraft of mass M moving at velocity v, known as thrust (T), is equal and opposite to the time derivative of linear momentum of the propellant [1].

$$T = M\frac{dv}{dt} = -\frac{d(m_p v_{ex})}{dt} \tag{1}$$

where m_p is the mass of the ejected propellant and v_{ex} is its exhaust velocity. In the idealized model where this velocity is equal for all the ejected mass and constant, the thrust can be written as [1]:

$$T = -v_{ex}\frac{dm_p}{dt} \tag{2}$$

The mass of the spacecraft includes the delivered mass (m_d) and the propellant mass (m_p), and changes due to the consumption of the propellant [1]:

$$M = m_d + m_p \tag{3}$$

$$\frac{dM}{dt} = \frac{dm_p}{dt} \tag{4}$$

Therefore, from (1) and (2):

$$M\frac{dv}{dt} = -v_{ex}\frac{dM}{dt} \tag{5}$$

or

$$dv = -v_{ex}\frac{dM}{M} \tag{6}$$

This can be integrated from the initial velocity v_i to the final velocity v_f, where the mass M changes from $m_d + m_p$ to m_d:

$$\int_{v_i}^{v_f} dv = -v_{ex}\int_{m_d+m_p}^{m_d} \frac{1}{M}dM \tag{7}$$

$$\Delta v = v_f - v_i = v_{ex}\ln\left(\frac{m_d + m_p}{m_d}\right) \tag{8}$$

The so called rocket equation, (8), shows that the change in velocity that some amount of propellant enables scales linearly with the exhaust velocity given by the chosen propulsion method, and logarithmically with any extra propellant added. Therefore, adding more and more propellant will bring diminishing results in terms of Δv, as opposed to an increased exhaust velocity, with which it scales linearly.

As a measure of thrust efficiency, specific impulse (Isp) is commonly used. By definition [1]:

$$Isp = -\frac{T}{\dot{m}_p g} \tag{9}$$

where $\dot{m}_p$ is the propellant flow rate, and g is the acceleration of gravity at earth's surface, $9.807 m/s^2$, which gives to the specific impulse the peculiar unit of seconds. By substituting (1):

$$Isp = \frac{v_{ex}}{g} \tag{10}$$

The specific impulse is linearly proportional to the exhaust velocity. In other words, as in (8), a propulsion method with higher exhaust velocity will be more efficient, and will be necessary to enable missions that require a high Δv to reach further parts of the solar system [1].

2.2 Electric propulsion

Although a large number of electric propulsion methods exist, some varying wildly from others, in general, any propulsion technology that uses electricity to achieve high exhaust velocity can be considered part of this group. Electric thrusters have exhaust velocities of around 10^2 to 10^3 km/s, depending on the propellant of choice, much higher than the 3 to 4 km/s exhaust velocities of chemical rockets [1]. This makes electric propulsion a highly efficient choice, which requires a lower propellant mass to perform a certain mission, and therefore enables the use of cheaper launch methods or frees mass budget for other components. However, electric propulsion also offers a much lower thrust than its chemical counterpart, typically of some fraction of a Newton, requiring longer burn times when performing orbital manoeuvres and making it unsuitable for certain jobs, such as overcoming earth's gravity and getting any payload to orbit [1].

Among the different electric propulsion methods that exist, two have gained higher popularity in recent times: ion and Hall thrusters. These have been used primarily for insertion and station-keeping in satellites, and as the primary propulsion source in several scientific probes [2-4]. Although a number of alternative propellants exist, xenon has become the preferred option for most, mainly due to the ease of handling inert gases and to the extra thrust that comes from a propellant consisting of heavier atoms [1].

2.2.1 Ion thruster

Ion thrusters, arguably the most well known among the electric propulsion methods, consist of first ionizing the propellant in some way and then accelerating it with an electrically charged grid. The higher the potential at the grid, the faster the velocity to which the ions will be accelerated to. This voltage can exceed 10 kV in some designs, offering a very high specific impulse ranging from 2000 to 10000 s, at the highest efficiency for an electric thruster from 60% to 80% [1].

Ion thrusters consist of three main parts: the plasma generator, the accelerator grids, and the naturaliser cathode. In the example shown in Figure 1, the xenon is ionized by electron discharge by the positively charged cathode. These ions are accelerated by the very negatively charged accelerator grids, forming the thrust beam. The naturaliser cathode outside of the thruster expels electrons at the same rate as ions, neutralizing them. If these ions were not neutralized, the spacecraft would accumulate a net electric charge, attracting positive ions from the plume. This would result in reduced acceleration and could damage other components of the spacecraft [1].
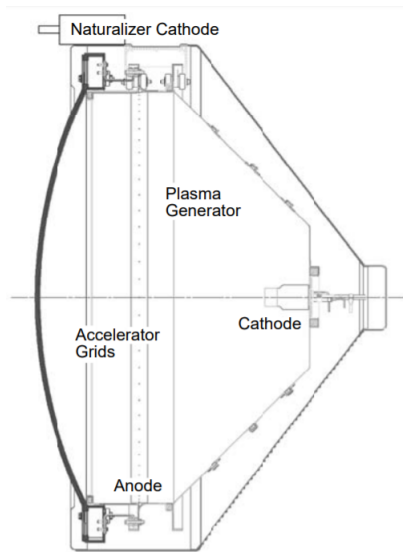
Figure 1: Ion thruster schematic. Obtained from [1].

In thrusters with different plasma generating techniques, such as microwave or radio frequency plasma generators, the design of the thruster is broadly speaking the same. They share the same basic distribution of plasma generator, accelerating grids and neutraliser cathode. The final performance of the thruster will mainly be conditioned by the efficiency of the plasma generator and the accelerator grids' design [1].

2.2.2 Hall thruster

Hall thrusters, as their name indicates, make use of the Hall effect to generate the plasma. An electric field parallel to the thrust axis accelerates ions and electrons in opposite directions, while a perpendicular magnetic field in the radial direction induces an spiral motion increasing ionization. They offer lower efficiency and specific impulse than gridded ion thrusters, but the device itself is much simpler, it can operate with fewer power supplies, and gives higher thrust [1].

A Hall thruster's general distribution also shows cylindrical symmetry along the thrust axis. On one end, the disk-shaped anode also acts as the gas feed. As found in the ion thruster, a hollow cathode outside of the spacecraft releases electrons. Some of these get directed towards the anode by the generated electric field, but they encounter a radial magnetic field, perpendicular to their motion, that inhibits their motion towards the anode. In their induced spiral motion in the $\mathbf{E} \times \mathbf{B}$ direction, they form the Hall effect current that gives the device its name, and get an increased chance of collisions with the released gas atoms. The propellant ionized by these electrons get accelerated in the opposite direction by the electric charge, and get neutralized by other electrons released by the cathode. An schematic of this process is shown in Figure 2. The performance of the thruster will be dependant on the shape and material of the discharge
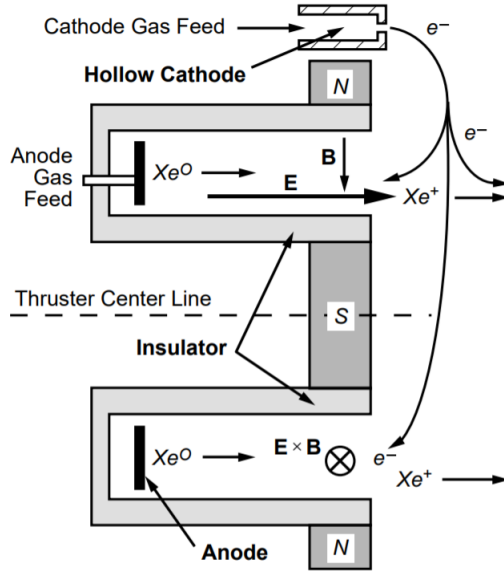
region and the details of the magnetic field [1].

Figure 2: Hall thruster schematic. Obtained from [1].

3 The ORBITA project

3.1 Overview

At its conception, the ORBITA project was envisioned to further advance state-of-the-art technologies that could potentially enable in-orbit diagnostics on electric thrusters in real time. This would allow to give feedback on the performance for fine tuning, increasing the lifetime of the thrusters or improving their efficiency during operation. The technical objectives of the program combine in the aim to increase the Technology Readiness Level (TLR) of in-flight diagnostic systems up to TLR 4, as defined by ESA: to reach breadboard functional verification in a laboratory environment. It was supported by the UK Space Agency and the European Space Agency, the second of which also founded the project and offered their facility and equipment [5].

The first step in ORBITA was taken in March 2018, and involved market analysis and the definitions of the requirements. The market analysis considered the potential market available to a fully developed ORBITA system. Information was provided with respect to the market opportunity and size, customers, competitors and product differentiation. Meetings were held with prospective customers so that input into the system's requirements could be provided. The key inputs were that ion velocity, Isp and thrust were the main thruster performance indicators of interest.

In the requirements definition, ion velocity was identified as the plume parameter of most interest, since it allows a determination of the thruster specific impulse. A full list of system requirements was also generated on which the hardware solution was then based. These requirements included the emission lines of interest (484.5, 504.5, 526.2 nm and 302.4, 326.9, 362.4 nm), thruster ion energy range accounted for (100-1850 eV); and ultimate Isp resolution (50 s).

A series of increasingly detailed trade-offs were performed on different diagnostic techniques, which resulted in a Langmuir probe and Fabry-Pérot interferometry as the selected choices for ORBITA I and ORBITA II respectively, two different versions of the system. The first would focus on spacecraft interaction effects, and the second one in plume measurement parameters. A third version, ORBITA X, would combine the two.

ORBITA II was chosen for a first breadboard model, due to its higher complexity. A full design culminated in a custom optical system and a mechanical structure appropriate for testing it in a vacuum chamber with a thruster, as well as the development of the software required to run it. Since this is the only version that was developed, every further mention in this document to the ORBITA system refers to ORBITA II.

3.2   Optical system

The ORBITA system relies on light to infer the desired information. As such, a way to collect the light was needed to be developed, that would pass it through the mirror plates that define a Fabry-Pérot interferometer, to finally be measured. The optical system responsible of this is described here. My personal job in this part of the project was to aid in the design as needed, and to choose components from manufacturers to fulfil the design, ensuring their compatibility.

The optics hardware in the ORBITA system can and has been separated into two distinct parts: The collection branch and the detection branch, shown respectively in Figures 3 and 4. The first, as its name states, collects light emitted by the plume and focuses it into a fiber optic, connected to the detection branch: the interferometer.

The collection device consists only of three optical components. A wide convergent lens, indicated in Figure 3 as 1, collects as much light as possible from the plume and focuses it onto the second lens. This divergent lens, 2, collimates the collected light. The light, now in the form of parallel rays, enters the mirror collimator, which directs it onto the fiber optic cable.
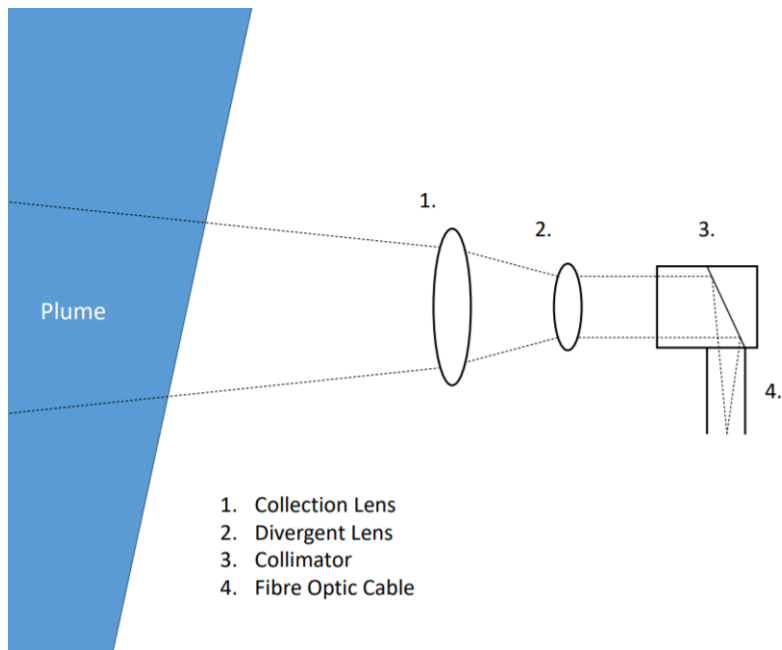
Figure 3: Schematic of the optical components that constitute the collection branch.

The optical fiber takes the light and directs it to the detection branch. An identical collimator as that found in the previous branch, 2 in Figure 4, now focuses the light exiting the fiber back to infinity. The surface it encounters first at 45° is the dichroic beam splitter, 3. The special coating in this component is such so that light of shorter wavelength than a certain threshold is reflected, whereas light of longer wavelength is transmitted. In our case, this separates xenon's ultraviolet and visible emission lines into two very similar branches, each optimized for its wavelength range. However, the transmitted visible light must first go through a compensator, 4, to be realigned with the rest of components, correcting the displacement produced by the beam splitter. The next major component the light encounters in its path are the bandpass filters 5, designed to select just a single emission line out of all coming from the xenon plasma. To select different lines, each branch has three distinct filters, placed in a filter wheel to make interchanging them easier.

All done to the light prior to this is so it comes into the etalons, 6 and 7, collimated and monochromatic. They have a custom coating optimized for the wavelengths selected to be observed. Depending on the angle of these, which can be adjusted with the rotation stages holding them, only a certain set of wavelengths will be transmitted. In other words, our monochromatic beam will only be transmitted when the etalon is at some determined angles to it, depending on its wavelength. Finally, any light that has been transmitted is focussed with lens 8 into the photomultiplier tubes, 9. These are extremely sensitive devices that essentially count the number of photons that reach it. These were chosen instead of alternatives such as charge-coupled devices (CCDs) because of how dim of a light source plasma plumes were expected to be.
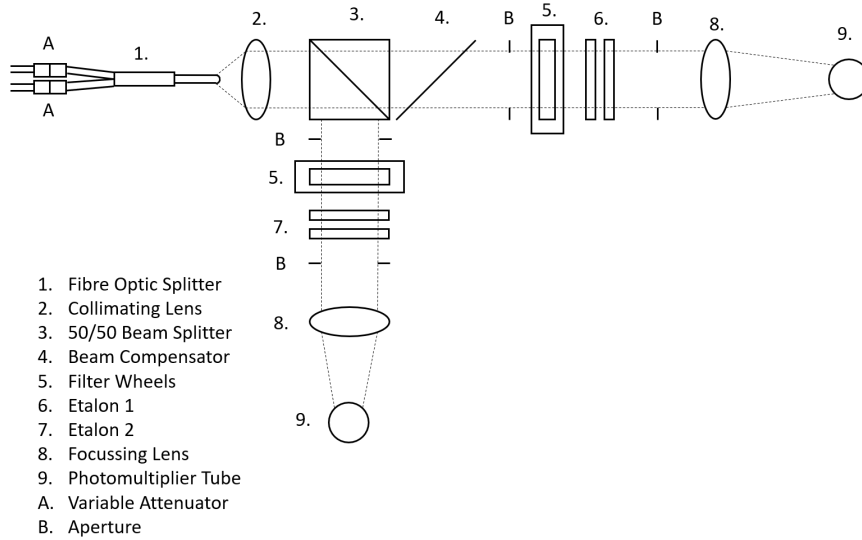
1. Fibre Optic Splitter
2. Collimating Lens
3. 50/50 Beam Splitter
4. Beam Compensator
5. Filter Wheels
6. Etalon 1
7. Etalon 2
8. Focussing Lens
9. Photomultiplier Tube
A. Variable Attenuator
B. Aperture

Figure 4: Schematic of the optical components that constitute the detection branch.

3.2.1 Fabry-Pérot interferometer

The detection side of the optical system is a Fabry-Pérot interferometer. Considering this is a key component of ORBITA, it is important to understand what this means and how it works. A Fabry-Pérot interferometer consists of two flat planes which create an optical cavity. The two surfaces have a high reflectivity, making the cavity act as an optical resonator, where multiple reflections occur causing interference depending on the optical path difference. In this way, the interferometer allows transmission of light at well-defined wavelengths [6].

An etalon is a type of Fabry-Pérot interferometer where the gap between the mirrors is fixed [6]. This is what is used in ORBITA. In our case, the gap is filled with air, and the optical path difference is tuned by rotating the etalons, which changes the beam incidence angle, resulting in a different distance path being taken by the beam between the mirrors. The path difference can be calculated with help of Figure 5.
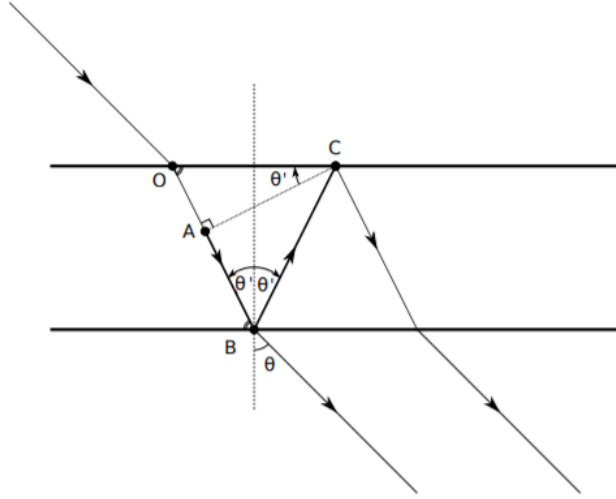
9

Figure 5: Illustration of the optical path difference between two adjacent rays. In our case, since the gap is filled with air, θ' is equal to the incidence angle, θ. Obtained from [6].

Following the illustration in Figure 5, the path difference is $\overline{ABC}$. This can be proven to be [6]:

$$\overline{ABC} = 2d\cos\theta \tag{11}$$

where d is the distance between the mirror surfaces. Therefore, the phase difference due to the optical path for light of wavelength λ [6]:

$$\delta = \frac{4\pi}{\lambda}n'd\cos\theta \tag{12}$$

Following the notation in [6], n' is the refraction index in the volume between the mirrors. In ORBITA, this would be the refraction index of air. Depending on the mirror material, an additional phase difference may be added [6]. In ORBITA's case, however, this does not produce any changes.

Following this, and considering all the transmitted amplitudes and the interference between each other, the fraction of the final transmitted intensity (I_T) over the intensity of the first transmitted ray (I_0) can be calculated, assuming no light is absorbed by the mirrors [6]:

$$\frac{I_T}{I_0} = \frac{1}{1 + F\sin^2\dfrac{\delta}{2}} \tag{13}$$

10

The coefficient F is a function of the so-called effective finesse, and introduces all non-ideal effects [6].

If the intensity of the transmitted light is observed as a function of wavelength, it can be seen that this has several peaks, as it will be shown in Figure 9. These peaks appear at regular intervals, named free spectral range (FSR) [6, 7]. This distance has a value of [7]:

$$\text{FSR} = \frac{\lambda^2}{2n'd} \tag{14}$$

3.3 Mechanical System

Although the aforementioned optical design was envisioned for transitioning to a potential future flight-ready version easily, the components selected were ultimately for a breadboard model. This was also the case for the mechanical system. The ORBITA system contains two pieces of the collection branch, along with a single build of the detection branch.

The collection components, since they would always have to be mounted within a vacuum chamber in order to collect the light of a xenon electric thruster, had to be made even in the earliest versions in development with vacuum compatible components. Both sets of optics are identical except for the mounting bracket as the angled version is designed to be rotated by a stepper motor. One of them, oriented perpendicular to the thruster plume, collects light from ions with velocity orthogonal to it, and therefore the light collected by it will not be Doppler shifted. This serves as a baseline against which the light from the other collection device can be analysed. As seen in Figure 6, this second one is to be placed under the thruster at a 30 degree angle to the thrust axis. The light collected by it is coming from the plasma accelerated by the propulsion device, moving away from the optics, and therefore redshifted. The 30 degree figure for the angled collection device was chosen to optimize for measurement accuracy and light collected. The smaller the angle, the bigger the projected velocity of the ions is, and therefore the bigger the Doppler shift, which would make the processing of the data more accurate. At the same time, with smaller angles, the light collected would originate further away from the thruster, and therefore be of even lower intensity than that from the closest parts of the plume, since plasma density drops rapidly along the thrust axis.
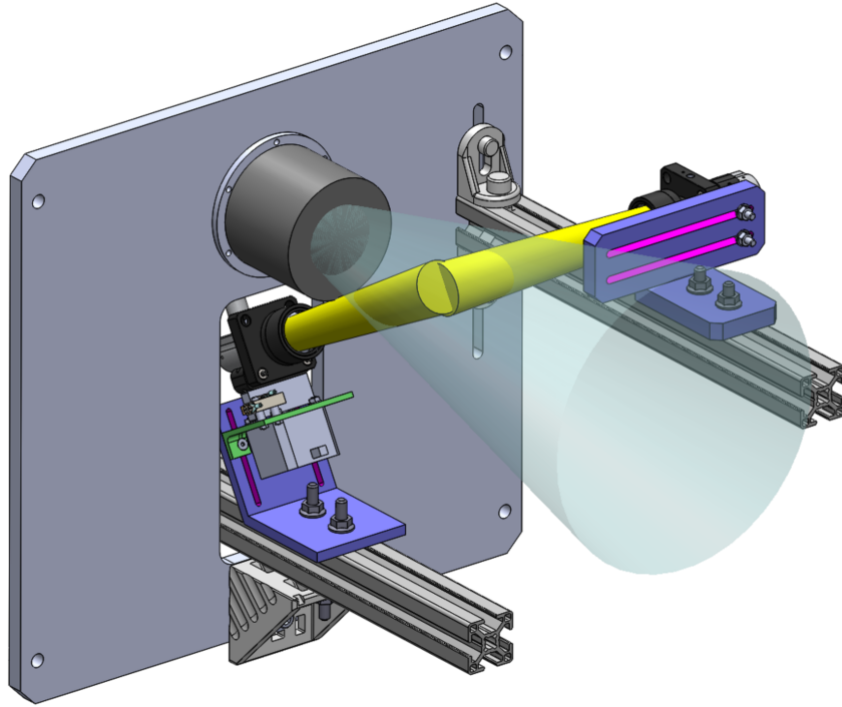
Figure 6: CAD drawing of the collection branch, assembled with a thruster. The yellow cones represent the field of view of the optical components, while the blue cone shows the thruster's plume. The grey box under the angled device is the stepper motor that rotates the device. The one on the right is the perpendicular collection device, while below the thruster the angled device can be seen.

As all of the collection assembly, the stepper motor and its adjacent components are vacuum compatible. This motor, controlled by an Arduino board placed outside of the vacuum chamber, rotates the optics to collect light coming from parts of the plume outside of the thrust axis. Even though this is not a critical part to achieve the main goal of the system–to measure ion velocity–it enables the measurement of another parameter in a relatively simple way: by integrating the collected light from each angle, it offers the plasma density distribution relative to the thrust axis, where it has its maximum. Therefore, the plume divergence can be calculated with a model of the plume density away from the thrust axis, as well as the ion velocities as a function of spatial distribution.

To control the angle of the optics, the Arduino is connected to an LCD screen outside of the chamber, as well as several buttons. It displays the current position of the motor, obtained by counting the steps previously taken, and with the buttons a target angle can be set to which it will rotate when asked to. Thanks to a switch next to the optics that is activated when the rotation reaches its limit to avoid collision with surrounding mounts, the reading of the position can be calibrated at any time. This is also done automatically every time it is

12

turned on, and counteracts the inaccuracies of the stepper motor in the form of missed steps that add together in long runs.

Light from both collection devices is carried though optical fiber, outside the vacuum chamber, to the detection branch, illustrated in Figure 7. These optical components are mounted on a breadboard, fixed with a custom cage system. The posts holding the etalons are screwed into precision rotation stages. By rotating these by fractions of a degree, only a set of wavelengths are transmitted through the etalons and reach the extremely sensitive photomultiplier tubes at the ends of the branch. In order to mitigate noise, and to protect these sensors that could be damaged by the light of the room, the whole component is encased in a box. The cables connecting the computer controlling the rotation stages and the photomultipliers, as well as the optical fibres, go into the box by throughputs, in order to mitigate stray light.
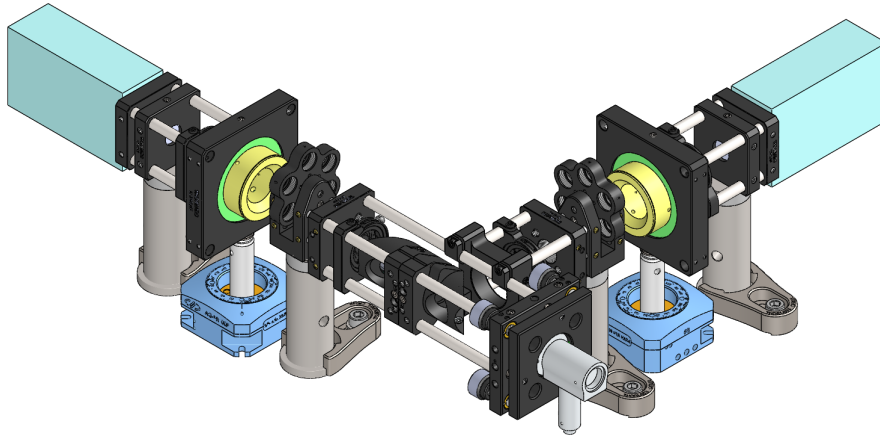
Figure 7: CAD drawing of the detection branch. The turquoise boxes represent the photomultiplier modules, the yellow cylinders the etalons, and in light blue are the rotation stages.

The Fabry-Pérot interferometer would allows to measure the difference of the wavelength of the light coming from each collection device, and therefore the velocity of the plume can be calculated.

Although my involvement in the design of the mechanical system was also secondary, giving advice when needed, I was responsible of developing the proof-of-concept version of the stepper motor subsystem.

3.4   Controller

Both photomultipliers and the rotation stages attached to the etalons must be connected to a computer to operate. Although they can be controlled manually with the software provided by the fabricators, the simple and repetitive tasks

they need to complete are plenty. It was therefore necessary to develop a program that would control these devices, log the data, and save it in a manner accessible for post-processing. This was achieved by a Python program that interfaces with the hardware via serial through USB, written in its entirety by me.

The photomultiplier module by Opto-Mechatronix comes with drivers that operate as a USB to serial. Upon installation, it can be operated by sending certain commands. To ease the development of the controller program, a python class was written that takes care of communicating with the device with the aid of the pySerial module, abstracting key functionalities of the photomultipliers (PMT) into simple functions. Moreover, it takes the task of initializing the communication port and readying the device before use. This involves reading a text file where different settings have previously been written, allowing the operator to choose the communication port to be used, the baudrate, the integration time of the device (i.e. the time the PMT spends counting photons for each measurement), and the state of the LED incorporated, all without having to look at the code. This approach offers an easy and straightforward tool for the development of the main program, while allowing the system to be operated with ease by any member of the team.

The state of affairs with Newport's *Agilis* rotation stage was relatively the same, and was therefore given a similar solution. A class handles the set-up of the communication ports and readies the device for operation, while abstracting the sending of commands into functions, with the settings on a text file.

When the main controller program is initiated, after the settings file have been completed as needed, the command prompt appears. All control by the operator on the program is done through here. The program asks the user to input which wavelengths are to be analysed, the voltage parameter of the thruster, which collection device is the light coming from and, if it is the angled device, what its angle is. Some of these parameters are necessary to run the program, such as the observed wavelength, while others like the thruster parameter are solely to differentiate the data from other runs when saved.

Two wavelengths are observed at the same time, one with each etalon, thanks to the beamsplitter that dissects the beam according to wavelength. After the photomultipliers and the rotation stages are initialized, etalon data provided by the manufacturers is loaded to determine, depending on the wavelength and the rotation step size chosen, how many steps each etalon needs to take. As its progress is displayed in the command prompt, the measurement loop is initialized. The rotation stage moves to the correct position, the photomultiplier is activated, data from it is requested, and then saved in its corresponding file. When the loop is finished, the rotation stages return the etalons to their initial position and the post-processing program is invoked, passing it the name of the file where the data has been saved.

3.5 Post-Processing

In order to aid the design for ORBITA, an approximate idea of what the etalon data would look like was needed. Therefore, a Python program to simulate the data expected to be received from the etalons was written at early stages of development by a colleague.

3.5.1 Etalon Trace Simulation

The designed system contains two branches in the detection side, each with an etalon optimized for three distinct wavelengths. For the first etalon, we choose to use the 526.2 nm, 504.5 nm, and 484.5 nm lines, and for the second one we use the 362.4 nm, 326.9 nm, 302.4 nm lines. The plume is measured in two places, first perpendicular to the thrust axis and then at an angle of 30 degrees to the thrust axis. These two measurements allow us to measure the rest wavelength of the plasma, and the Doppler shifted wavelength.
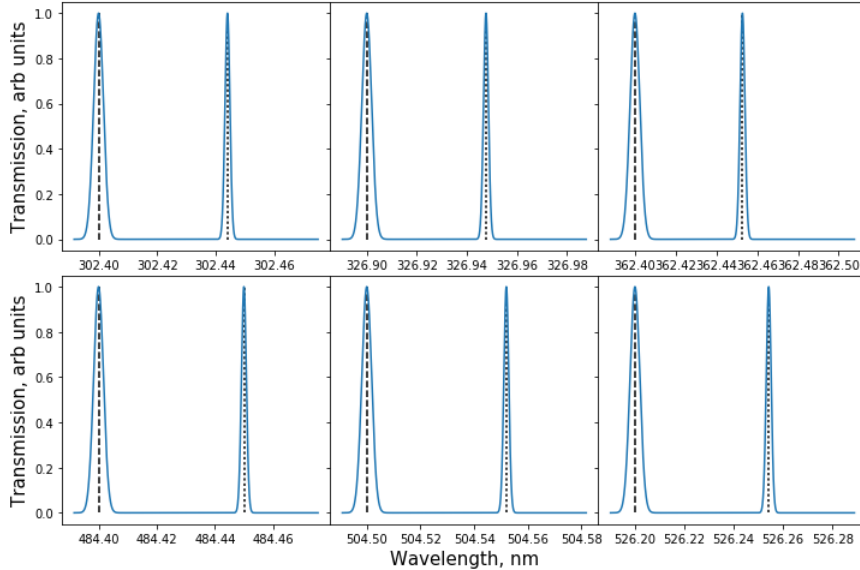
Figure 8: Simulated emission lines that reach etalon 1 (top row) and etalon 2 (bottom row) lines. Shown are the rest frame lines (dashed) and Doppler shifted lines (dotted).

Figure 8 shows the calculated emission of the six xenon ion emission lines. We assume an arbitrary emission intensity for each line. The rest frame lines are indicated with the dashed line in each plot, while the dotted lines indicate the Doppler shifts. For these lines, we have assumed an ion velocity of 35 km/s, inside the typical range of electric thrusters, and a Gaussian distribution of velocities around each line.

Each of these emission lines will be measured individually in the etalons. The lines are measured by scanning the etalon angle of incidence through a number

15

of free spectral ranges (FSR). The transmission function of the etalons is calculated and then the emission lines are passed at a range of incidence angles. Figure 9 shows an example of a transmission function, I_T/I_0 in (13).
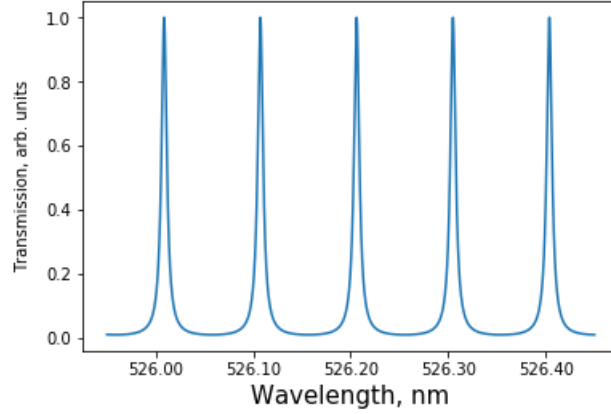

Figure 9: The transmission function of an etalon at a central wavelength of 526.2 nm.

The transmitted light ($F(\lambda)$) at some angle of incidence in then equal to:

$$F(\lambda) = S(\lambda)T(\lambda) \tag{15}$$

where $S(\lambda)$ is the signal function, shown in Figure 8, and $T(\lambda)$ is the transmission function. Figure 10 shows the transmitted light as a function of incidence angle (θ), for the 6 emission lines, with the etalon tilted through five FSRs. We calculated two transmitted signals, one for the rest frame wavelength measured perpendicular to the thrust plane, and one signal for the Doppler shift line.
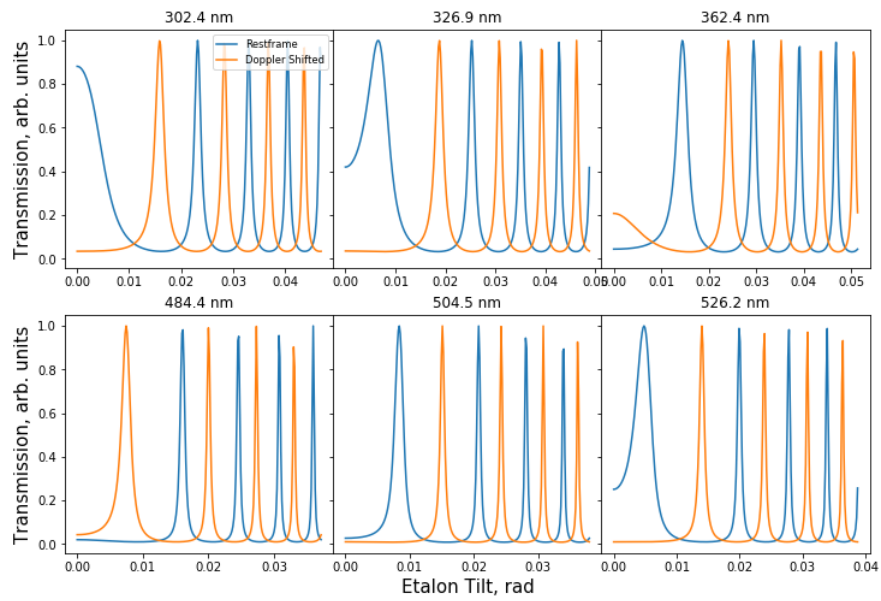
Figure 10: The transmitted signals through the etalons for the six emission lines to be studied. The blue lines are for the rest frame wavelengths, while the orange lines denote the Doppler shifted wavelengths. Each peak is separated by one FSR.

Finally, Figure 11 shows the etalon traces as is outputted by the program. We have applied a Gaussian noise to the signal, with a signal-to-noise ratio of 10, to account for the noise we would measure in testing and operation that the post-processing program should be able to handle.
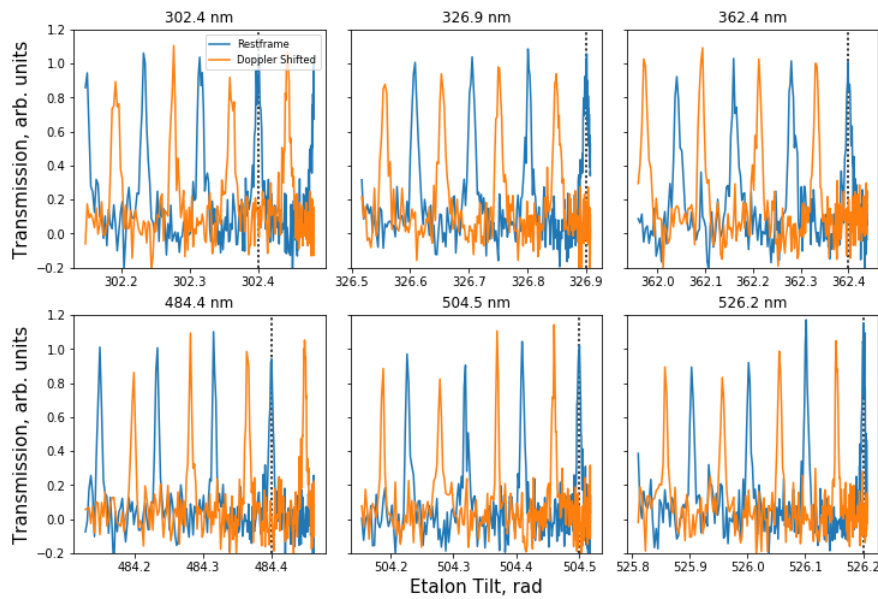
Figure 11: Final output of the etalon trace simulation for the six emission lines, with added noise. The blue lines are the signal from the rest frame wavelength, and the orange from the Doppler shifted line.

3.5.2 Post-processing: Peak Finding

Based on the simulated transmission lines from the etalons, I wrote the program that would process the measured data. Two version were eventually developed, following different methods to achieve the same goal. The first of these relies on peak finding.

To obtain the Doppler shift of the emission lines, transmission peaks must be identified among the data. For this, the *scipy.signal.find_peaks_cwt* function provided in the SciPy module for Python is used. This function first smooths the data using an estimated width of the peaks to be found, and then finds the peaks with wavelet transformation and returns those which comply with the optional parameters the user may have introduced.
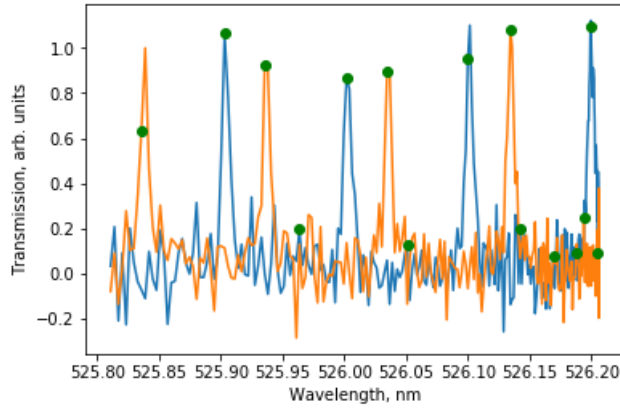
Figure 12: In green, the location of peaks found by the algorithm in the simulated transmission signal.

Figure 12 shows the direct result of the peak finding algorithm applied to the simulated data. As it can be seen, it locates various peaks among the noisy base which are not of our interest. Assuming the emission lines to be significantly brighter than the background, we have filtered this false positives by only considering those peaks higher than half the maximum transmission measured, as seen in Figure 13.
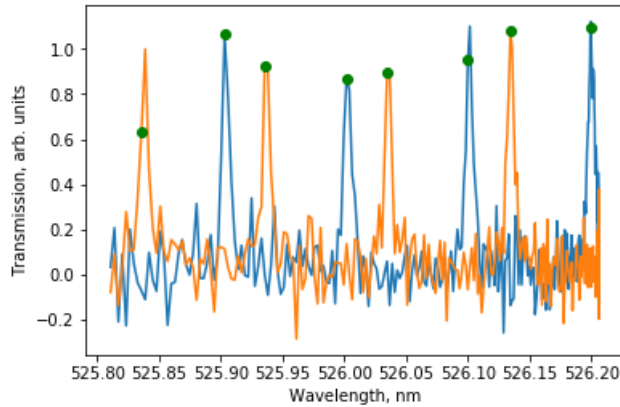

Figure 13: In green, the remaining peaks after applying the first filtering condition.

Having found the location of the emission lines in both the rest frame and Doppler shifted transmission signals, the next step is to pair them so we know which peaks correspond to the same emission line. Assuming that the interferometer is located behind the thruster plume, we know that the moving ions will be travelling away from the device, and therefore their signal will be redshifted. The Doppler shifted emission line will have a longer wavelength than its static counterpart. So, for each rest frame peak, its Doppler shifted "partner" will be

19

that which is closest to it with a longer wavelength. Those peaks for which a pair is not found are ignored from this point on, as shown in Figure 14.
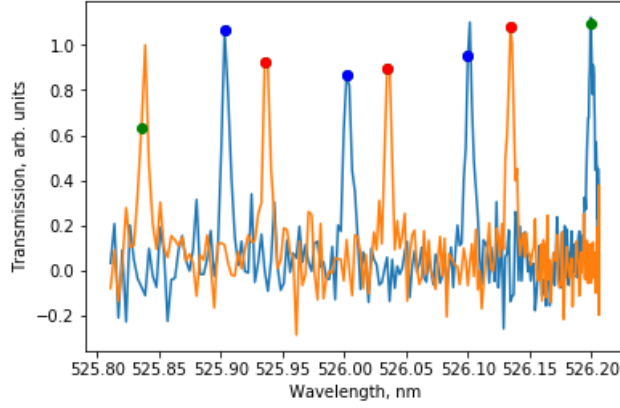

Figure 14: In blue and red, paired peaks from the rest frame and Doppler shifted transmission. The green peaks are unpaired. For each blue peak, its partner is the first red one to the right.

For each pair, the difference in wavelength between both peaks is the Doppler shift ($\Delta\lambda$). Taking the average for each pair, if the central wavelength is λ_0 , c is the speed of light and the viewing angle is α, the ion velocity [7-9]:

$$
v = c\frac{\Delta\lambda}{\lambda_0}\frac{1}{\cos\alpha} \tag{16}
$$

However, according to publications on similar experiments [8, 9], we could find non Doppler shifted emission lines even when taking measurements at an angle to the thrust axis, as illustrated in Figure 15. Therefore, another version of this program exists where both simulated transmission lines are added together.
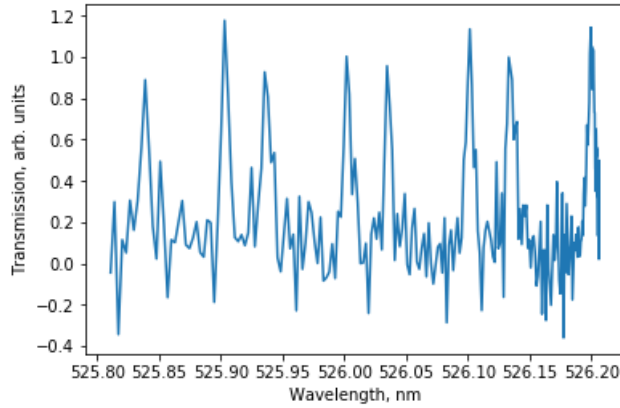
Figure 15: The same transmission lines as in Figure 12, added together.

In this case, we cannot directly differentiate the peaks originating from slow-moving ions and the Doppler shifted ones. However, we do know what the central wavelength is, that one of the static frame emission lines should be found there, and that because of the etalon's geometry, these peaks will be repeated in regular intervals of the same length as the free spectral range. Therefore, we can set where we should find the non Doppler shifted peaks, as shown in Figure 16.
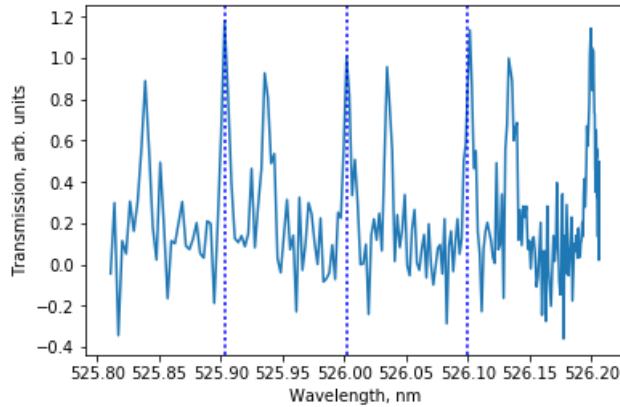
Figure 16: The blue dotted vertical lines mark the theoretical locations of the static frame emission lines.

In this case, the peak-finding works just the same way as previously explained. Once having located the peaks, the closest ones to the theoretical locations (inside a threshold distance) are considered to be the static frame emission lines, and so, the rest are Doppler shifted ones. This step is represented in Figure 17. With the peaks separated, the pairing and the calculation of Doppler shift and ion velocity are done just as shown above.
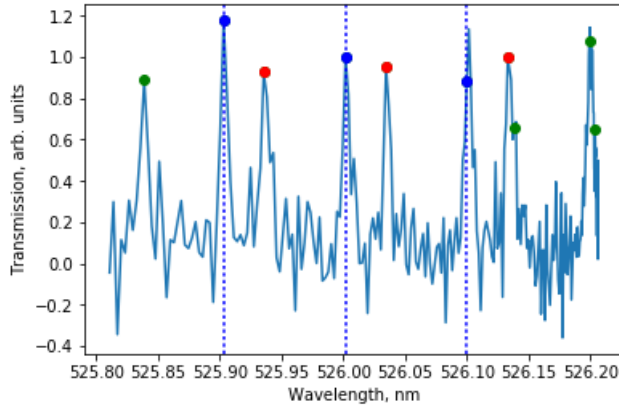
Figure 17: The blue dots, all closest to the theoretical locations calculated from the FSR, show the static frame emission lines, and the red ones their corresponding Doppler shifted pairs.

To test the reliability of the processing program, we tried increasing the noise of the simulated data. It was found that the results are acceptable up to a signal-to-noise ratio of 3.33, while in lower velocities ($\lesssim 25$ km/s) it can sustain a signal-to-noise ratio even lower than 2.5. However, increased noise level produces unfiltered mistakes from the peak finding algorithm, causing some considerably large mistakes in the velocity calculations. Although these are averaged out, they are still shown in increased error bars calculated from the standard deviation.

In any case, the first version described above responds considerably better to increasingly noisy data, so it can be said that having independent measurements for the static frame (perpendicularly to the thrust axis) and Doppler shifted (at an angle to the thrust axis) is highly preferable, even though it might not be possible when observing a plume on a vacuum chamber.

3.5.3   Post-processing: Gaussian Fit

In an attempt to improve upon the previous post-processing program, a second one was developed that achieves the same goal in a different way. The main difference to the previous one is that, instead of finding the peaks directly from the etalon data, it makes use of the fact that these peaks are repeated in regular known intervals to "fold" them, adding them together, as shown in Figure 18. In order to do this, the data needs to be interpolated to get a linear set of points in wavelength space.
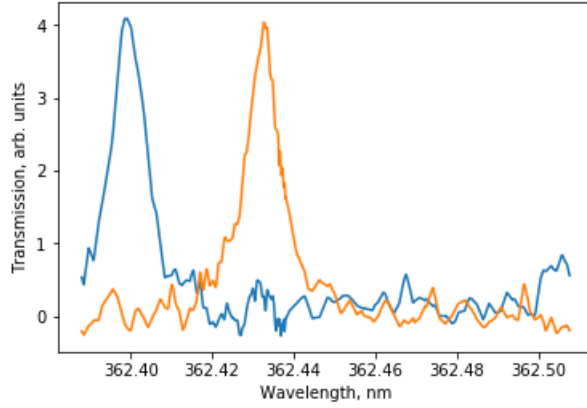
Figure 18: Folded etalon traces. In blue, the measurement taken perpendicularly, and in orange, the measurement taken at an angle.

A better defined peak and the fact that there is only one for each data set, allows us to make a Gaussian fit of the transmission lines, instead of just identifying the peaks, as seen in Figure 19.
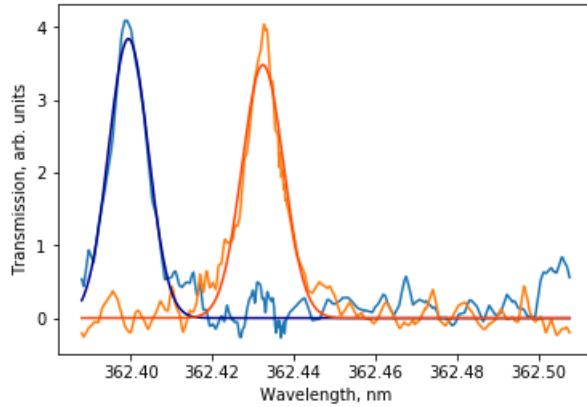

Figure 19: In dark blue and orange, the Gaussian fit for both data sets.

The Gaussian function is defined as:

$$g(x) = A \exp\left[-\frac{1}{2}\frac{(x-\mu)^2}{\sigma^2}\right] \tag{17}$$

In our case, μ gives the position of the centre wavelength, A is the amplitude in arbitrary units, and σ defines the width. Therefore, $\delta\lambda$ described previously as the distance between peaks is now $\Delta\mu$. The calculation of the ion velocity is now as straightforward as before. Moreover, the Doppler broadening (i.e. the

width of the peaks) is mainly caused by the ion temperature T_i [7, 8]. Knowing this, more information can be obtained on the plasma than with the previous method, with the following equation [8]:

$$T_i = m_{Xe} \left(\frac{1}{7.162 \times 10^{14}} \frac{\sigma\sqrt{8\ln(2)}}{\lambda_0} \right)^2 \tag{18}$$

where m_{Xe} is the mass of a xenon atom in atomic units and λ_0 is, as before, the central wavelength.

With this method, combining both signals presents us with a new challenge. Finding the Gaussian fit for two peaks in the same data set was possible, but it proved to be unreliable when both peaks were closer with lower ion velocities.
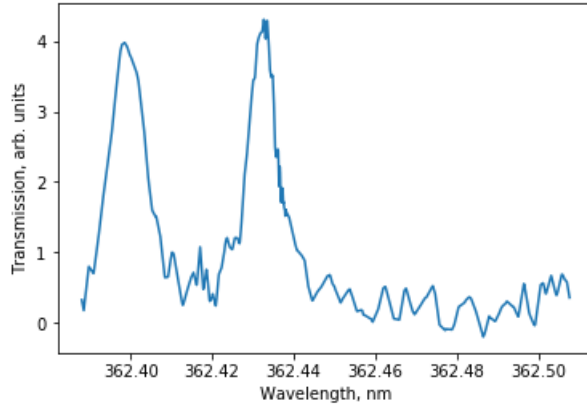

Figure 20: The same transmission lines as in Figure 18, added together.

To be able to reliably fit our peaks in Figure 20 with a Gaussian function, we have set an arbitrary limit under which we know the static frame peak will be, marked in Figure 21. This allows us to separate both peaks in what effectively are two different data sets, although it sets an artificial lower limit to the velocity we can measure. This is not an issue as big as it first might seem to be, since the lower limit under which by the Rayleigh criterion both peaks become undistinguishable is approximately the same.
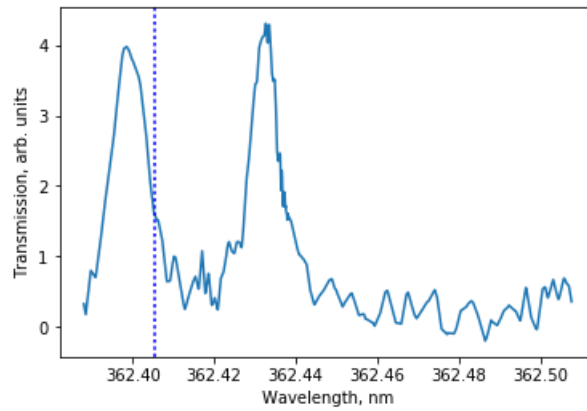
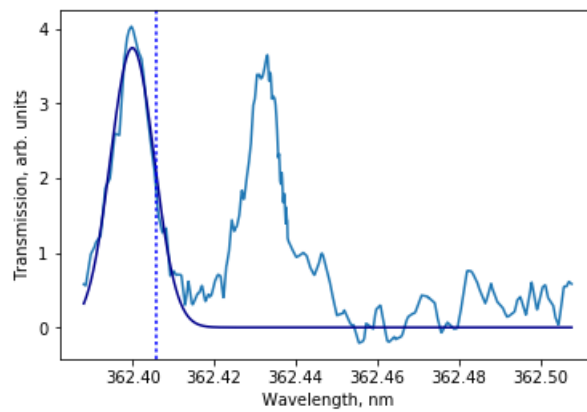Figure 21: The blue dotted vertical line marks the somewhat arbitrary limit set to separate the peaks.

Figure 22: With the peaks separated, the fit with a Gaussian function of the static frame peak is done in the same way.

Once we have identified the first peak, as shown in Figure 22, we can remove it from the transmission line by simply subtracting its value, as in Figure 23. As so, we isolate the Doppler-shifted peak, fitted in Figure 24.
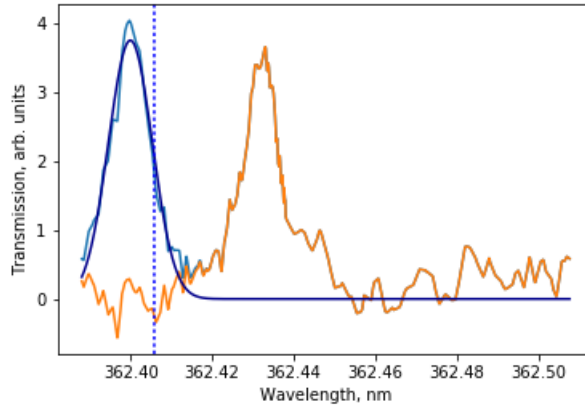
25

Figure 23: In orange, the transmission line after having removed the first peak.
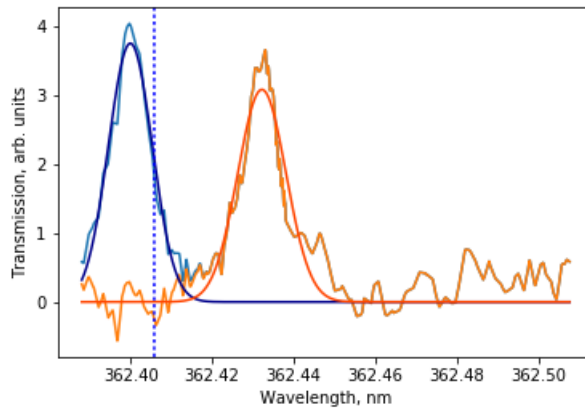

Figure 24: With only one peak in the data, the fit of the Doppler-shifted peak is done in the same way.

This method of subtracting both peaks was found the one to be most successful compared to other tested ones (f.e., using the same limit to find the second peak) when the ion velocity is low and both peaks start to overlap.

When testing this program with noisier signals, the results obtained are surprisingly positive. Although with increased uncertainty, if the perpendicular and angled transmission lines are treated separately, the program gives a correct measurement of the ion velocity with a signal-to-noise of as low as 2. When the peaks are combined, the minimum signal-to-noise ratio comes closer to 2.5. In any case, this is significantly better than the peak finding algorithm, with the added benefit of measuring the ion temperature too.

Although all figures show simulated measurements where the plume is moving away from the interferometer and therefore the emission lines are redshifted, all post processing programs have been written so that with a simple change can

be adapted to work in the opposite case, where the signal gets blueshifted.

3.6   Test

The breadboard model, built following the optical and mechanical designs shown above, for which the controller and processing programs were written, was tested in conjunction with ESA Propulsion Lab (EPL) in January 2019. They offered their facilities at the European Space Research an Technology Centre (ESTEC) in Noordwijk, Netherlands. EPL provided the mini-RIT thruster and the CORONA Vacuum Facility, and took the responsibility of operating them.

The mini-RIT, shown in Figure 25, is a miniature gridded ion thruster that uses xenon as propellant. It was used in testing as a xenon ion source to test the capabilities of the ORBITA system with ions at different velocities. A gridded ion engine was chosen due to the ability to change the ion velocities by varying the beam voltage. In the case of the mini-RIT, the voltage was expected to go as low as 500 V, and as high as 1900 V.

Figure 25: The mini-RIT gridded ion engine.

The CORONA test facility, shown in Figure 26, is a vacuum chamber located in EPL, mainly dedicated to Electric Propulsion thrusters testing activities. The size of the main vessel is 2 m in diameter and 4 m in length, the hatch size is 1 m in diameter and 1.5 m in length. The total volume is about 16 m^3. Three glass windows situated on the hatch (one on the front door and two on each side of the hatch) and two on the main chamber (on the side and one at the back of the facility) allow visually monitoring the devices under test. However, since our device relies on emitted light, these windows had to be covered while testing in order to mitigate stray light.

Figure 26: EPL's CORONA vacuum chamber at ESTEC.

The assembled ORBITA components were mounted along with the mini-RIT on a plate fixed to a trolley system CORONA has, as the schematic of Figure 27 illustrates. This trolley allows the components to be displaced from the main chamber into the smaller cavity on the side of the chamber. Since this smaller volume can be completely isolated from the main one, this becomes an extremely useful feature when the test components need to be extracted for service. The smaller volume can be re-pressurized, opened, and de-pressurized again in a matter of hours instead of days the whole chamber would take. The optical and electrical connections of the ORBITA device were made through the port in the small section on the chamber.
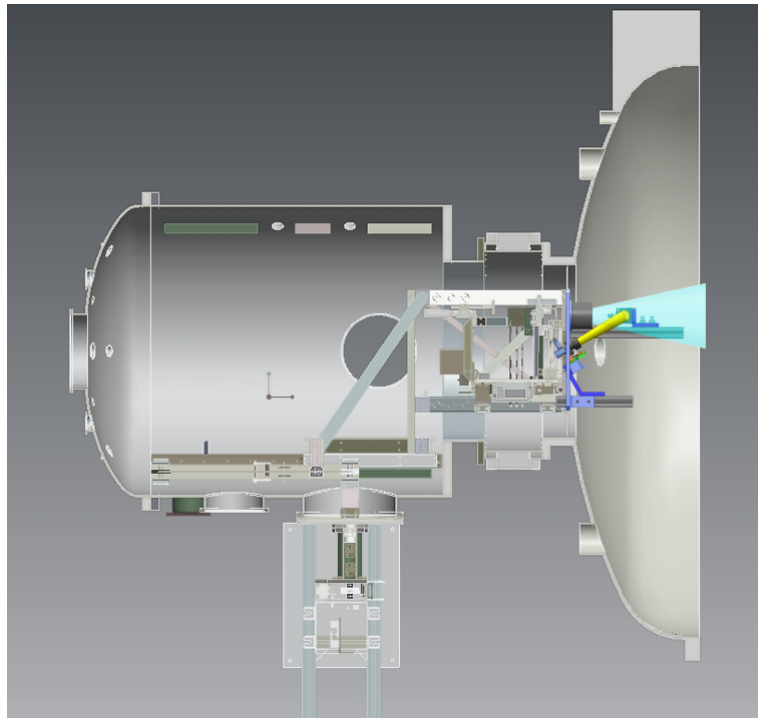
Figure 27: Schematic of the overall test set-up mounted inside the CORONA vacuum chamber. The light blue cone represents the thruster plume coming out of the mini-RIT, the yellow cones represent the field of view of the ORBITA collection devices, while in darker are their structural components.

For the ORBITA device, the objectives while testing were to observe the chosen xenon emission lines, to measure the velocity of the ions with reasonable accuracy, and to rotate to sweep the width of the plume in order to give velocity distribution and plume divergence measurements. The whole test sequence is represented in Figure 28, showing both tasks performed by EPL personnel of selecting different thruster parameters for the mini-RIT, and AVS UK personnel on the ORBITA device. Once the thruster is turned on, different parameters were selected. With a first run of measurements taken, an appropriate integration time was selected on the photomultipliers for the current parameters. A larger integration time gives less noisy measurements, but greatly increases the test duration. With the correct settings, the real measurements were taken and automatically processed, including the sweep across the plume, and the data was saved. "Etalon-PMT subroutine" represents the Python program explained above responsible of controlling the etalon rotation stages and of taking measurements from the photomultiplier tube.
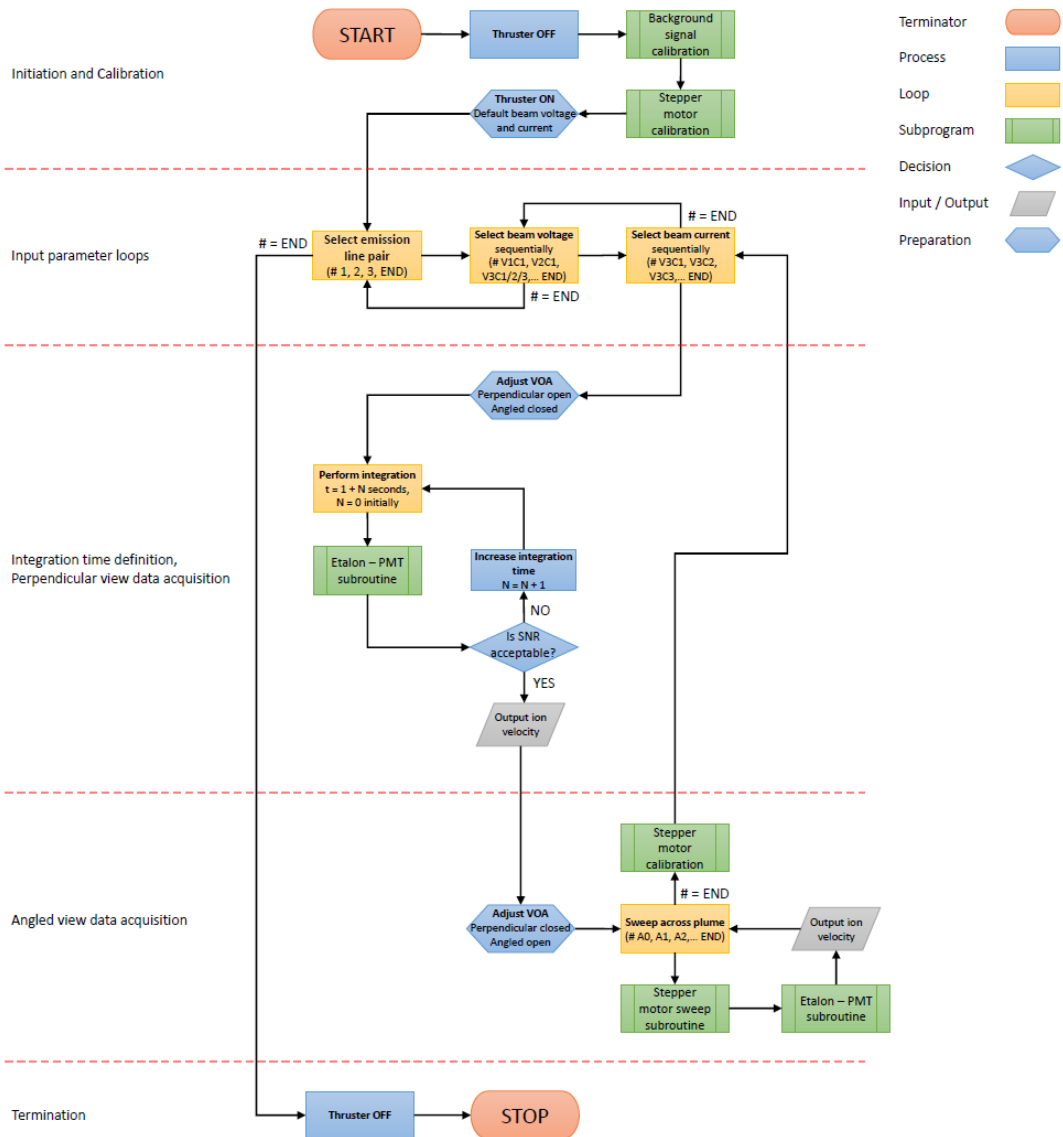
Figure 28: The test sequence developed to test ORBITA.

3.6.1 Test results

During the testing, I unfortunately could not travel to ESTEC as was first planned due to changing schedules. However, I did offer remote support to the colleagues there, and was involved in the decision making processes that took place. As the test begun and the first results were plotted, it became clear that the signal-to-noise ratio obtained was considerably worse than expected. The controller program could move the rotation stages in as it should, the photo-multipliers were recording data and transmitting it to the computer, this data was being saved and read by the post-processing program as expected, and all other components were working correctly. However, the obtained data lacked

the regularly repeated peaks expected from the etalon interference pattern. Although the processing program claimed at times to have fit a Gaussian curve to the data, nothing more than random noise could be extracted, as shown in Figure 29.
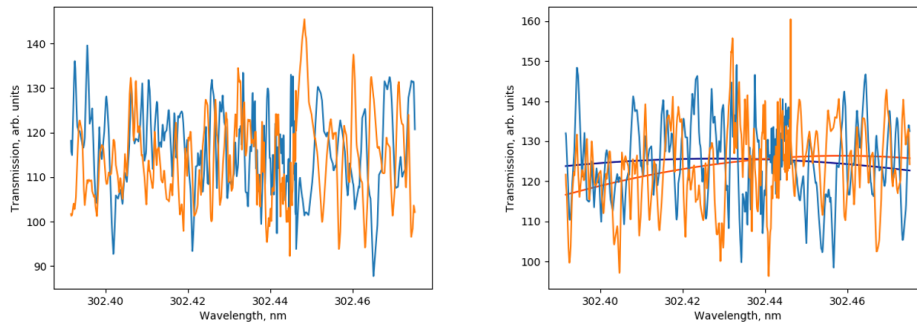

Figure 29: Measurements obtained during different runs of testing. Both show random noise, even though the processing program has tried to obtain a result from the one on the right.

Different causes were considered for this results. Levels of light generated by the mini-RIT could have not been high enough, or we could be observing light from the residual gas that was overwhelming light from the thrust beam. Other potential causes investigated included light scattered off interior chamber surfaces and ambient light reaching into the photomultipliers outside of the chamber, despite suppression methods taken beforehand.

In order to overcome the aforementioned potential sources of lack of meaningful data, several measures were taken. To increase the light received, thruster parameters were modified. To reduce the noise level against the signal, the integration time of the photomultipliers was increased. If the source of the noise was the light scattered inside the chamber, using CORONA's trolley system to pull the thruster back inside the smaller cavity of the system should have changed the background environment enough to produce significant changes in the data. However, none of these actions made any noteworthy improvement.

At this point, ESA provided a Mercury-Argon light source much brighter than the thruster plume to test the etalon configuration. One of the UV emission lines of this light source at 302.15 nm was sufficiently close to one of the xenon emission lines the system was designed for, at 302.4 nm. The filter responsible for isolating this emission line has a full width at half maximum of 1.5 nm. The light source was connected to the ORBITA detection branch through optical fiber, using an attenuator to prevent damage to the sensitive photomultipliers.

The data taken using this light source, showed some more promising results. As shown in Figure 30, by operating the rotation stages manually and recording the data on a much wider range than what the Python program was doing, peaks similar to what was expected were found, at approximately the same distance
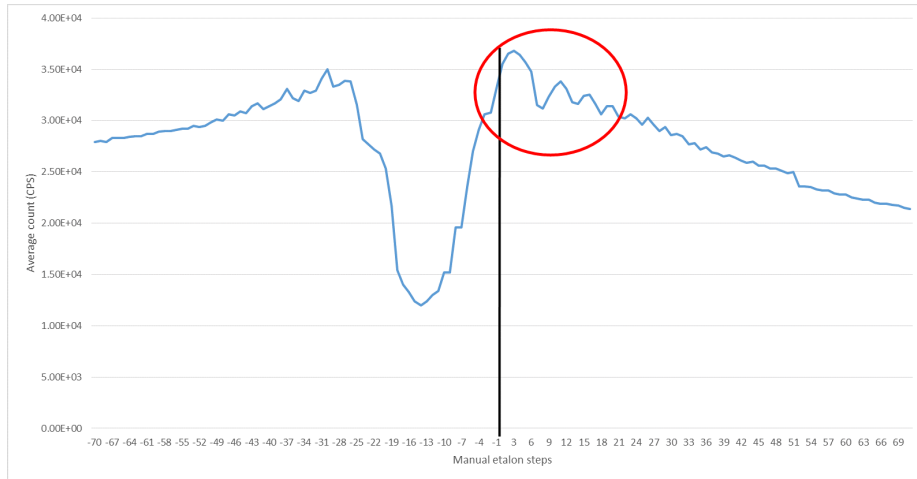
to each other as predicted.

Figure 30: Manually obtained results using the light source at a wide range of etalon angles. The black vertical line marks the 0º angle, an in red are encircled the peaks previously mentioned.

During the design process, the idea of using pinholes behind the etalons was considered. Although the decision at the time was that it would not be necessary after consulting experts, the negative results of the test made the idea to be reconsidered. Repositioning a variable aperture iris to act as a pinhole between the etalon and the photomultiplier, the manual data acquisition was repeated. The results showed a positive change from the previous dataset, where the etalon peaks were more prominent, as shown in Figure 31. Moreover, it was also determined that the range at which the peaks appear was narrower than expected, and it could be possible to miss them in the automatized runs due to inaccurate etalon alignment methods used.
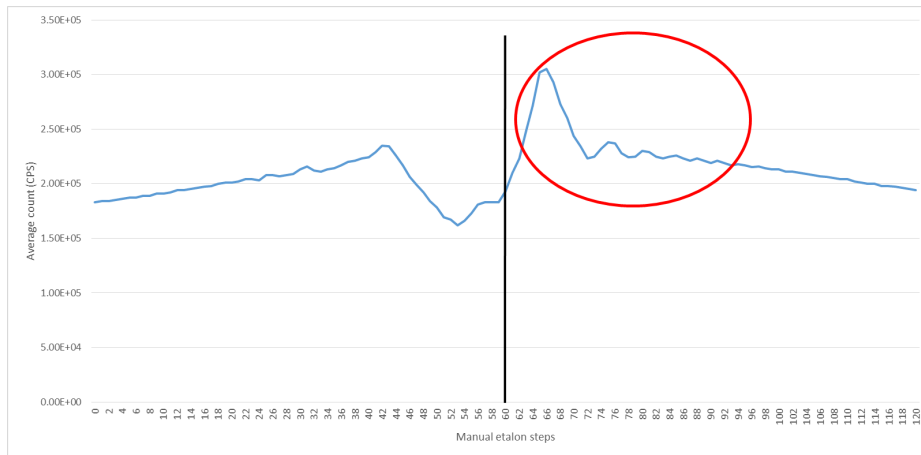
Figure 31: Manually obtained results using the light source at a wide range of etalon angles, including a pinhole between the etalon and the photomultiplier. The black vertical line marks the 0º angle, an in red are encircled the peaks mentioned.

All in all, the system was unable to find static nor Doppler-shifted emission lines in test runs using the thruster, and was therefore impossible to give a reading of ion velocity. However, the later runs using the light source did leave some room for optimism. The key issues of the system were determined to be the lack of light reaching the photomultipliers an the absence of a pinhole in the design of the system, and potentially etalon misalignment as well.

4   Conclusions

In summary, the bulk of my job in ORBITA centred on software development. I managed to send and receive messages through serial with Python, to interact with different hardware. I successfully wrote a program that automatically takes and saves large amounts of data from the interferometer, a second one that processes the data without any external input, and managed to integrate one with the other. The controller program proved its worth in testing, where it considerably reduced the time needed for each measurement run without introducing any drawbacks. Unfortunately, no real data was measured that the processing program could analyse. However, the developed program did perform extremely well with the simulated data, where it managed to reliably and accurately extract the ion velocity even from very noisy data.

About the project overall, at light of the results obtained, the actions necessary to rectify the issues found were identified. These include a re-design of the detection side of the optical system where a pinhole is included. Potentially, this could be done by an optics engineer experienced in Fabry-Pérot interferometers, since this was the first time working on such a system for all members of the team. Moreover, the criticality of the alignment of the etalon needs to be fully investigated, and an improved alignment method found from the results of this

33

investigation. The new design will need to be tested with a xenon light source with all emission lines that are used by the system before being fully tested with a thruster again. Finally, it needs to be determined whether the light levels reaching the photomultipliers can be increased, even considering testing with another thruster that generates more light. So, even though the results of the testing were not those that we had hoped for, there is still room for optimism that ORBITA could be made to work.

5 References

[1] D. Goebel and I. Katz, *Fundamentals Of Electric Propulsion* (Wiley, Hoboken, N.J., 2008).

[2] https://www.spacex.com/sites/spacex/files/starlink_press_kit.pdf

[3] S. D. Clark, M. S. Hutchins, I. Rudwan, N. C. Wallace, J. Palencia and H. Gray, in *the 33rd International Electric Propulsion Conference* (2013).

[4] https://solarsystem.nasa.gov/missions/dawn/overview

[5] http://sci.esa.int/sci-ft/50124-technology-readiness-level

[6] L. Giovannelli, Study Of A Fabry-Pérot Interferometer Prototype For Space Applications, Master Thesis, Universita degli studi di Roma Tor Vergata, 2011.

[7] F. Zander, S. Löhle, T. Hermann and H. Fulge, Journal Of Physics D: Applied Physics 50, (2017).

[8] D. Gawron, S. Mazouffre and C. Boniface, Plasma Sources Science And Technology 15, (2006).

[9] S. Mazouffre, P. Lasgroceix, N. Claire and D. Pagnon, in *the 4th International Spacecraft Propulsion Conference* (2004).